The Innovation, Volume *3*

Supplemental Information

Achieving metal-like malleability and ductility in $Ag_2Te_{1-x}S_x$ inorganic thermoelectric semiconductors with high mobility

Huiping Hu, Yuechu Wang, Chenguang Fu, Xinbing Zhao, and Tiejun Zhu

Supplemental Information

Achieving metal-like malleability and ductility in $Ag_2Te_{1-x}S_x$ inorganic thermoelectric semiconductors with high mobility

Huiping Hu,[1] Yuechu Wang,[1] Chenguang Fu,[1,*] Xinbing Zhao,[1] and Tiejun Zhu[1,*]

[1]*State Key Laboratory of Silicon Materials, and School of Materials Science and Engineering, Zhejiang University, Hangzhou 310027, China*

*Corresponding author.

E-mail addresses: chenguang_fu@zju.edu.cn (Chenguang Fu), zhutj@zju.edu.cn (Tiejun Zhu)

Supplemental Information

Supplemental Information including:

Materials and Methods

Figures S1 to S7

Note 1

Supplemental Materials and Methods

Synthesis of quenched and annealed sample To synthesize the quenched samples, raw elements Ag (99.9%, shot), Te (99.999%, chunk), and S (99.999%, powder) were weighted according to the stoichiometric $Ag_2Te_{1-x}S_x$ ($x = 0 \sim 0.5$) into quartz tubes and sealed under high vacuum. To protect the tubes from the explosion, the heating rate was set slowly during the melting process. Firstly, the tubes were heated to 773 K at the rate of 2 K min^{-1}, held at this temperature for 4 h, and then heated to 1073 K at the rate of 1 K min^{-1}, held at this temperature for 4 h, and then heated to 1273 K at the rate of 0.5 K min^{-1}, kept at this temperature for 12 h in a chamber furnace. Subsequently, the tubes were quenched in cold water to obtain final quenched ingots. For obtaining the annealed samples, the quenched ingots were sealed in tubes with evacuating to 10^{-3} Pa, annealed at 723 K for 7 days to facilitate the formation of cubic phase, and naturally cooled to room temperature in the furnace. The quenched and annealed ingots were used for studying TE and mechanical properties. In addition, to obtain the furnace-cooled ingot, the sample was heated to 1273 K at the same heating rate as the quenched sample, held for 12 h, and naturally cooled to room temperature in the furnace.

Characterization The phase structure of all samples was characterized by an X-ray diffraction system (XRD, PANalytical, Aeris DY866) equipped with a high-temperature stage using Cu Kα radiation (λ = 1.5406 Å). The variable temperature XRD patterns were recorded following the heating protocol between 323 K to 773 K. The microstructure and elemental distribution

were characterized by field emission scanning electron microscopy (SEM, Hitachi, SU-8010) equipped with energy-dispersive X-ray spectroscopy (EDS) and electron probe microanalysis (EPMA, JOEL, JXA-8100) with a wavelength-dispersive spectroscope (WDS). Differential scanning calorimeter (DSC, TA, Q200) measurements were performed in nitrogen flux to investigate the phase transition with a heating rate of 5 K min^{-1}. Uniaxial compression tests and tensile tests on the bulk specimens were carried out on a universal machine (Siomt, JVJ-20s) with a loading rate of 0.5 mm min^{-1}. The cuboids in the size of 3 × 3 × 6 mm^3 were used for compression tests and dog bone-shaped specimens (7 × 20 ×1 mm^3) processed by wire cutting were used for tensile tests. The electrical conductivity σ and the Seebeck coefficient S were simultaneously measured between 300 and 573 K on a commercial Linseis LSR-3 system in a helium atmosphere. The total thermal conductivity κ was calculated via $\kappa = D \times C_p \times \rho$, where the thermal diffusivity D was measured by laser flash method (Netzsch, LFA457) and the density ρ was measured by the Archimedes method, and the specific heat capacity C_p was estimated using the Dulong-Petit value. The Hall carrier concentration n_H and Hall mobility μ_H were calculated by $n_H = 1/eR_H$ and $\mu_H = \sigma R_H$ respectively, where e is the unit charge, R_H is the Hall coefficient which was measured by a Mini Cryogen Free Measurement system with the magnetic field varying from -4 T to 4 T.

Supplemental Figures

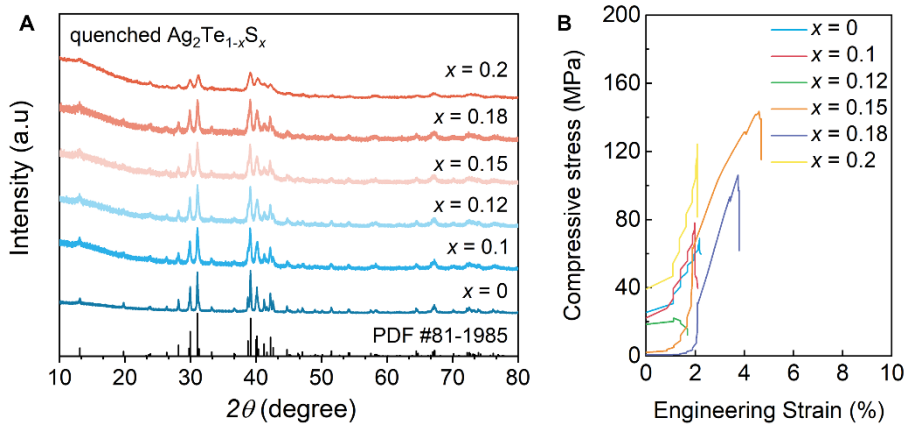

Figure S1. Crystal structure and mechanical properties of quenched $Ag_2Te_{1-x}S_x$ ($x \leq 0.2$). (A) Powder XRD patterns. (B) Compressive stress-strain curves.

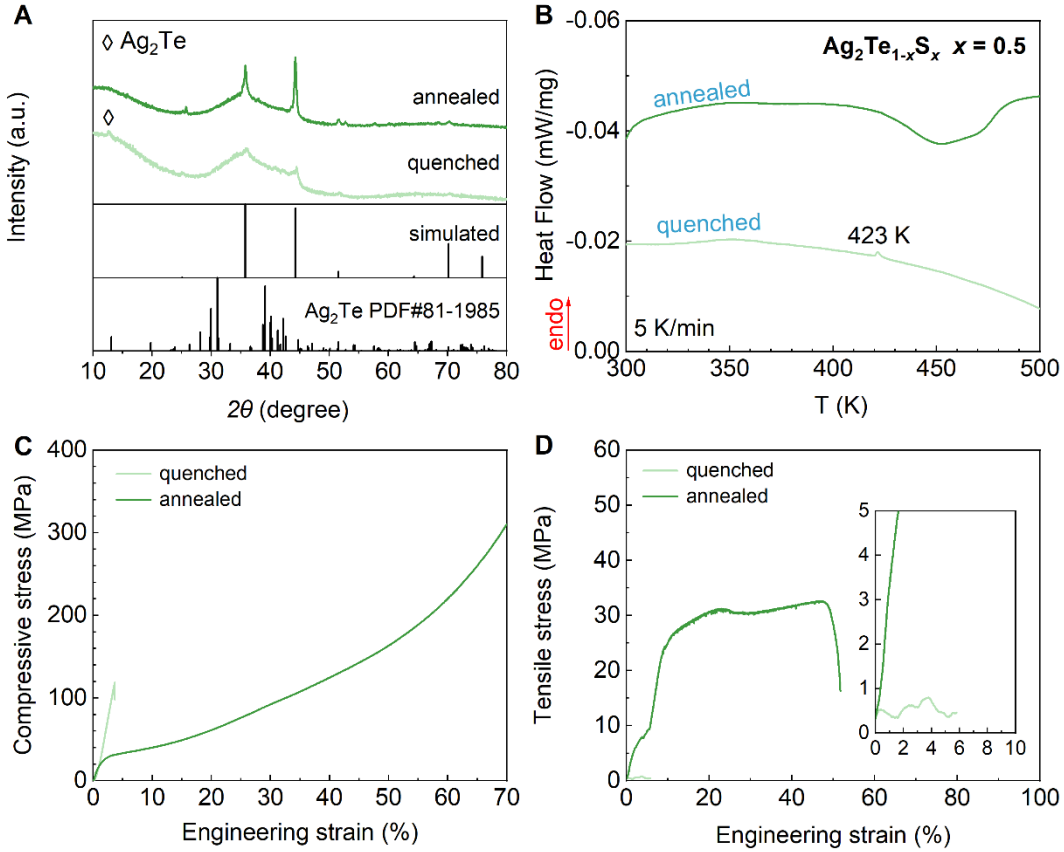

Figure S2. Elimination of monoclinic Ag_2Te phase in inorganic semiconductor $Ag_2Te_{0.5}S_{0.5}$. (A) Room-temperature bulk XRD patterns of the quenched and annealed $Ag_2Te_{0.5}S_{0.5}$ samples. The simulated patterns by VESTA are displayed for comparison. (B) DSC heating curves for quenched and annealed $Ag_2Te_{0.5}S_{0.5}$ samples with a heating rate of 5 K/min. Stress-strain diagrams for quenched and annealed $Ag_2Te_{0.5}S_{0.5}$ samples in the compressive test (C) and the tensile test (D).

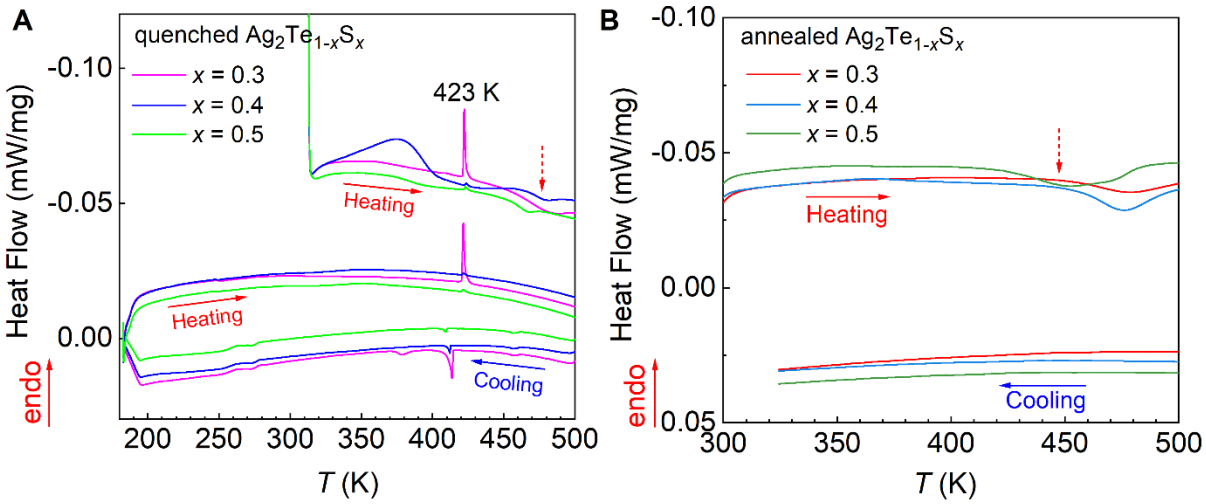

Figure S3. DSC curves for quenched and annealed $Ag_2Te_{1-x}S_x$ specimens with a heating rate of 5 K/min. (A) Quenched $Ag_2Te_{1-x}S_x$. The curves of the first heating cycle for the quenched specimens have been shifted up along the Y axis to avoid overlapping with other measured curves. (B) Annealed $Ag_2Te_{1-x}S_x$.

Broad bumps around $2\theta = 30–50°$ in the bulk XRD results (Figure 2C) reveal the partial amorphization of the $Ag_2Te_{1-x}S_x$ materials. In order to detect the glass transition of the solid amorphous phase in $Ag_2Te_{1-x}S_x$, which is an endothermic step change occurred in the heating DSC traces, low-temperature DSC curves for quenched $Ag_2Te_{1-x}S_x$ are displayed in Figure S3A. The process of the thermal scan for the low-temperature DSC curves is firstly heating to the set temperature, then cooling to the low temperature (200 K), and heating to the set temperature from the low temperature again. No clear glass transitions are observed in the DSC traces of the quenched specimens. A slight dip, which is only observed in the first heating cycle of the thermal scan for all the quenched and annealed $Ag_2Te_{1-x}S_x$ samples, might be due to the crystallization of the amorphous phase. However, the wide exothermic peaks of the crystallization around 450 ~ 500 K are irreversible, and cannot be detected in the following cooling and reheating process.

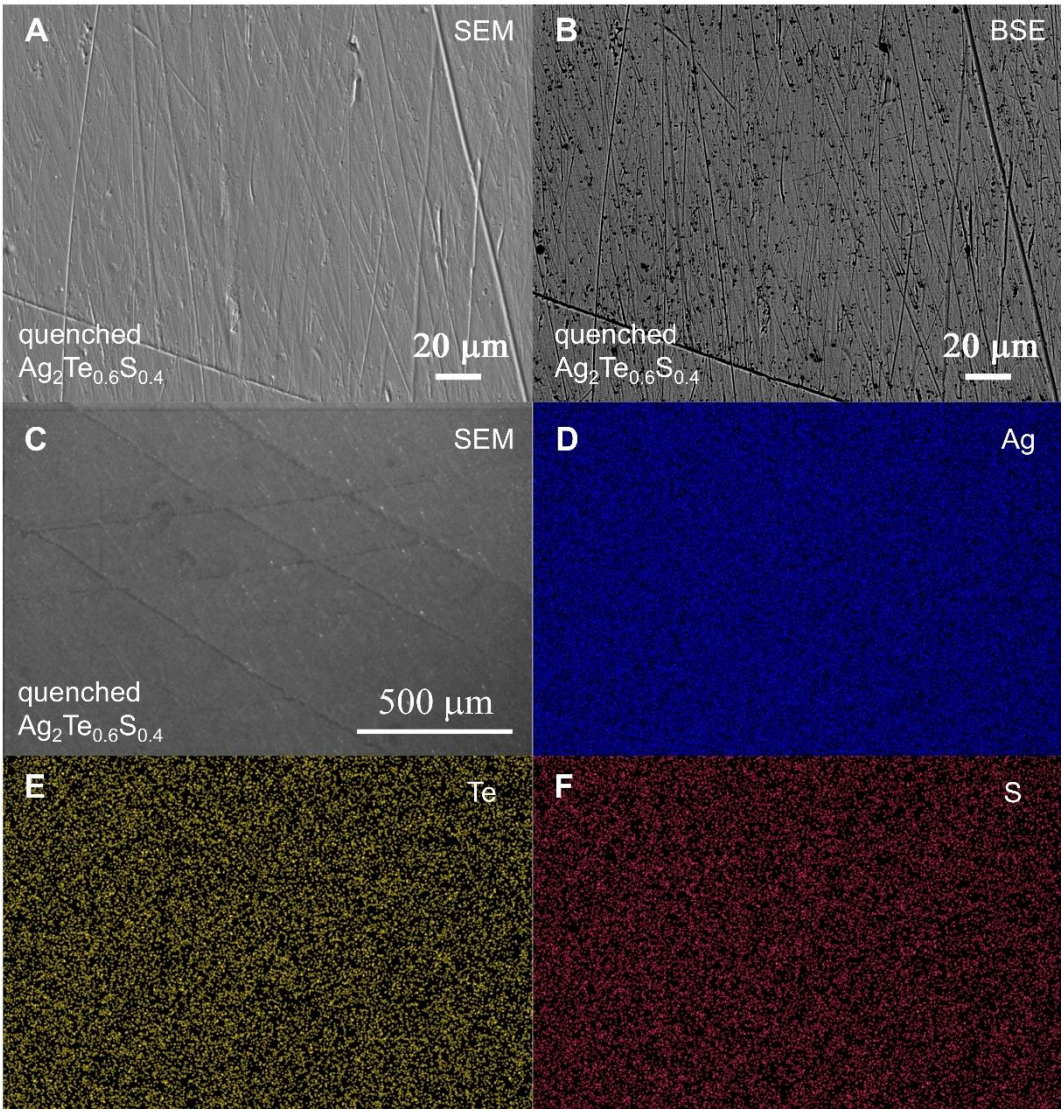

Figure S4. Microstructure of quenched $Ag_2Te_{0.6}S_{0.4}$ sample. (A) EPMA secondary electron image, and (B) EPMA backscattered electron image of the polished surfaces. (C) SEM images of the polished surface. (D) Ag, (E) Te and (F) S elemental distribution in (C).

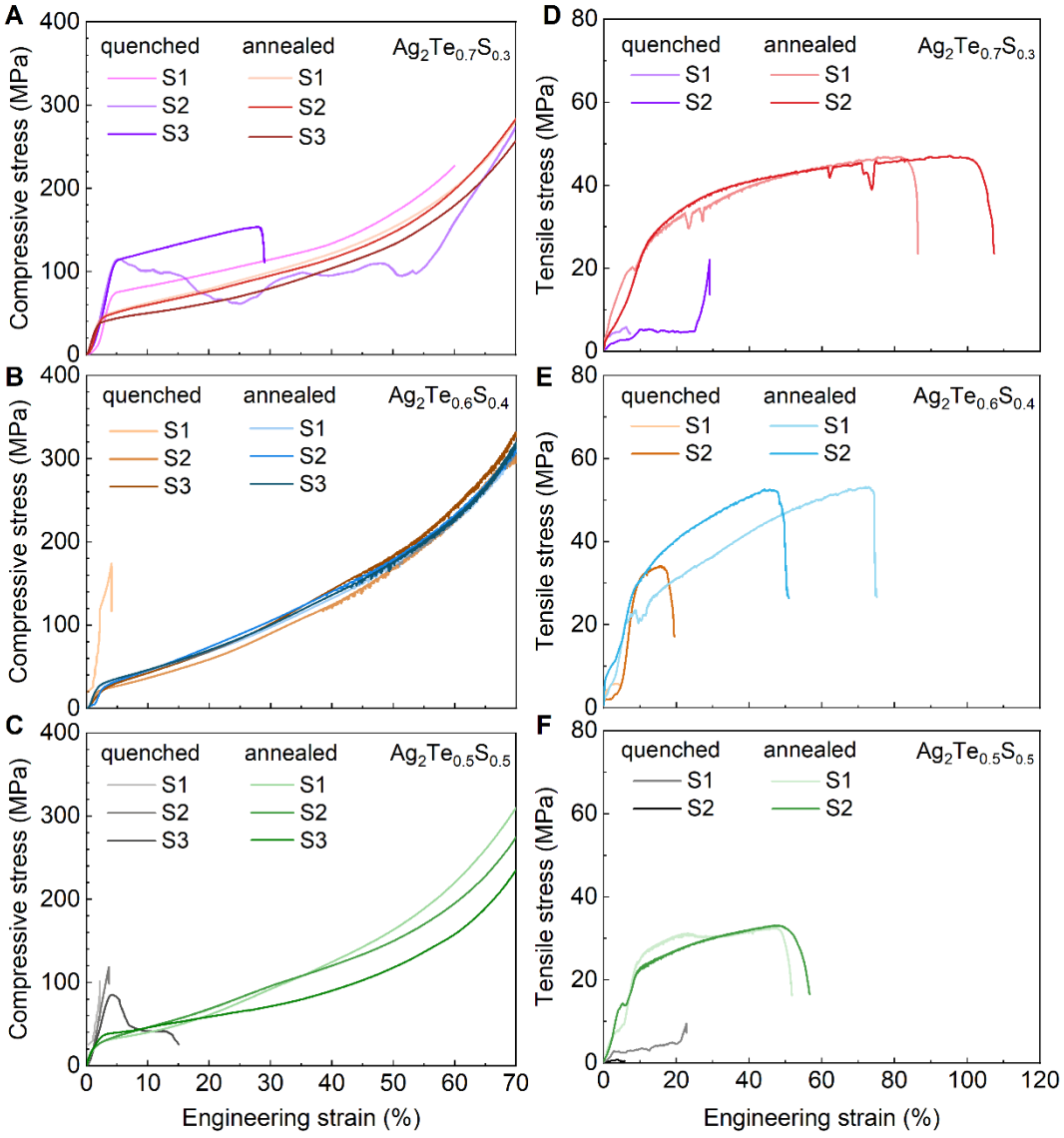

Figure S5. Reproducibility and stability of mechanical properties for inorganic semiconductor $Ag_2Te_{1-x}S_x$ (x = 0.3, 0.4, and 0.5) Stress-strain diagrams for quenched and annealed $Ag_2Te_{1-x}S_x$ specimens in the compressive test (A), (B) and (C) and the tensile test (D), (E) and (F). S1, S2 and S3 indicate the measured specimens processed from the same ingot.

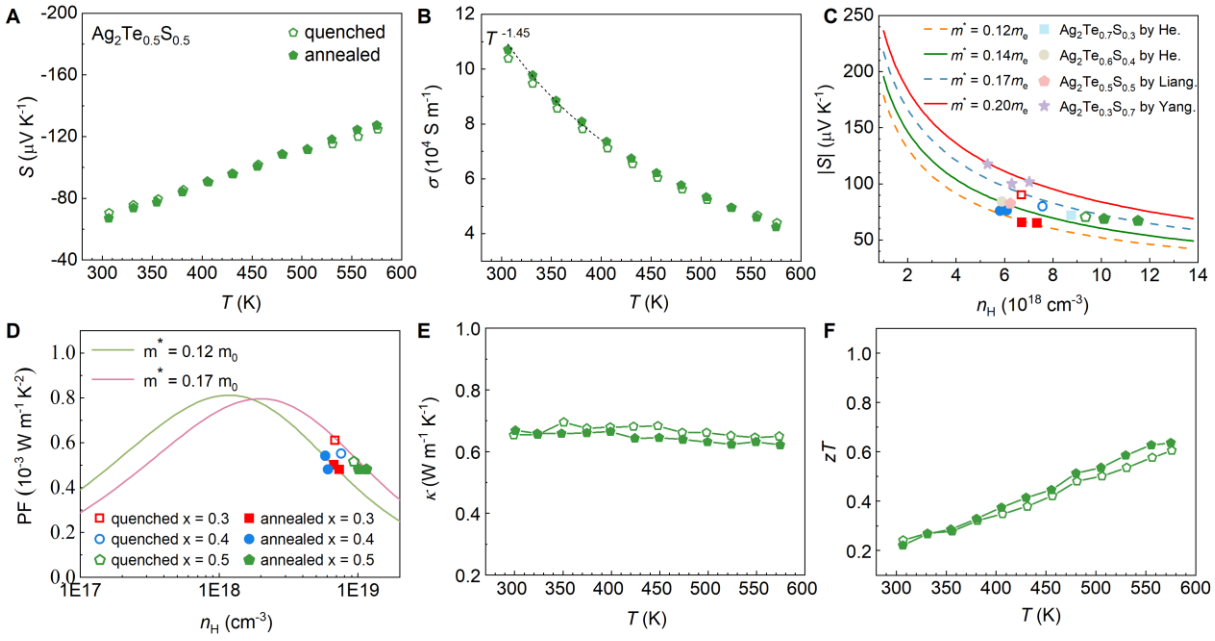

Figure S6. Temperature dependence of thermoelectric properties for inorganic semiconductor $Ag_2Te_{0.5}S_{0.5}$ (A) Seebeck coefficient S and (B) electrical conductivity σ for quenched and annealed $Ag_2Te_{0.5}S_{0.5}$. (C) Pisarenko plots for $Ag_2Te_{1-x}S_x$ (x = 0.3, 0.4 and 0.5) specimens, the lines are calculated by the SPB model with different density-of-states effective mass m^*. The data for $Ag_2Te_{0.7}S_{0.3}$[1], $Ag_2Te_{0.6}S_{0.4}$[1], $Ag_2Te_{0.5}S_{0.5}$[2], and $Ag_2Te_{0.3}S_{0.7}$[3] reported previously are added for comparison. (D) Carrier concentration dependence of power factor PF for quenched (hollow symbols) and annealed (solid symbols) $Ag_2Te_{1-x}S_x$ (x = 0.3, 0.4, and 0.5) at 300 K. The curves are generated by SPB model. (E) Total thermal conductivity κ and (F) zT values for quenched and annealed $Ag_2Te_{0.5}S_{0.5}$.

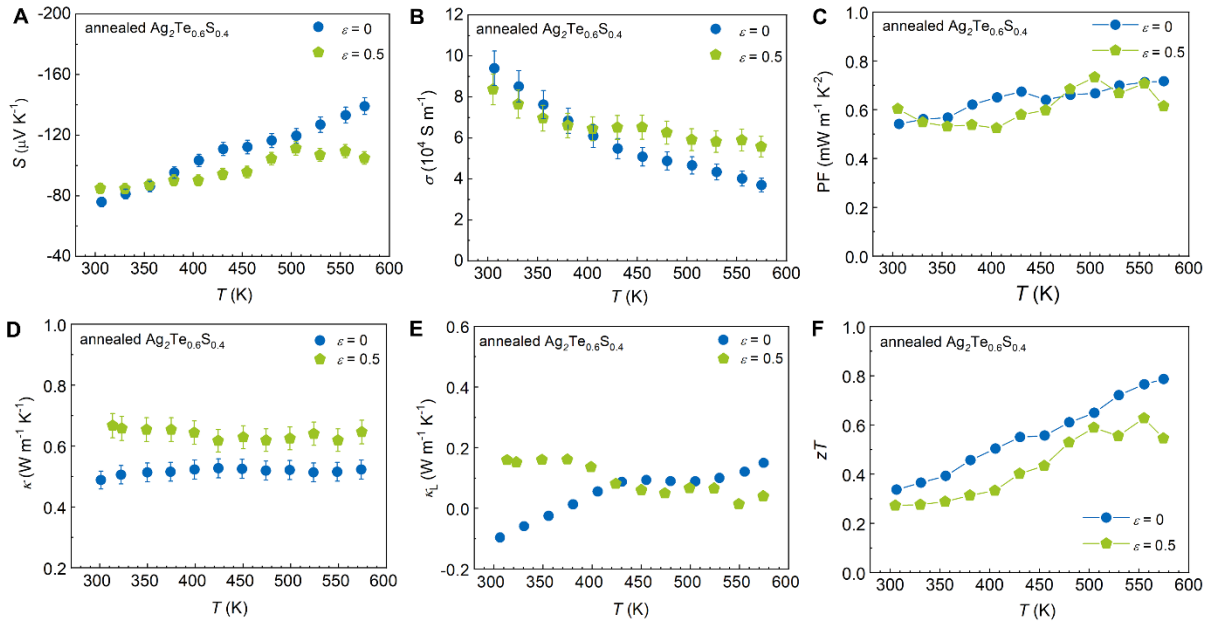

Figure S7. Effect of compressive deformation on the thermoelectric properties of plastic annealed $Ag_2Te_{0.6}S_{0.4}$ sample. Temperature dependence of (A) Seebeck coefficient, (B) electrical conductivity, (C) power factor, (D) total thermal conductivity, (E) lattice thermal conductivity, and (F) zT values.

The most significant variation is that the thermal conductivity increases with the increasing compressive strain ε. Considering that the values of the Seebeck coefficient and the electrical conductivity at room temperature are almost unchanged, the increased thermal conductivity of $\varepsilon = 0.5$ sample should mainly originate from the increased lattice thermal conductivity. For metals and alloys, the mechanism of plastic deformation is slip and twinning, and the density of dislocations will increase drastically during plastic deformation, which may contribute to a reduction in lattice thermal conductivity. However, the anomalous increase of lattice thermal conductivity with the introduction of compressive deformation in annealed $Ag_2Te_{0.6}S_{0.4}$ suggests that the plastic deformation mechanism of $Ag_2Te_{1-x}S_x$ materials is independent of the movement of dislocations

Supplemental Note 1

Single parabolic band (SPB) model. The electrical transport properties of $Ag_2Te_{1-x}S_x$ were analyzed using the SPB model obtained from the Boltzmann transport equation within the relaxation time approximation. Assuming the acoustic phonon scattering limits the carrier mobility and the minority carrier transport is negligible, the related parameters can be expressed below

$$F_i(\eta) = \int_0^{\infty} \frac{x^i}{1+\exp(x-\eta)} \mathrm{d}x \tag{1}$$

$$S = -\frac{k_B}{e}\left(\frac{2F_1}{F_0} - \eta\right) \tag{2}$$

Where η is the reduced Fermi level, k_B is the Boltzmann constant, e is the magnitude of charge of an electron or hole, F_i is the Fermi integral, and S is the Seebeck coefficient.

$$r_H = \frac{3}{2} F_{1/2} \frac{F_{-1/2}}{2F_0^2} \tag{3}$$

$$n_H = \frac{4\pi(2m_d^* k_B T)^{3/2} F_{1/2}}{h^3 r_H}$$

Where r_H is the Hall factor, m_d^* is the DOS effective mass, h is the Plank constant, T is the absolute temperature, and n_H is the Hall carrier concentration.

$$\mu_H = \mu_0 \frac{F_{-1/2}}{2F_0} \tag{4}$$

$$PF = S^2 n_H \mu_H e \tag{5}$$

Where μ_0 is the SPB mobility parameter, μ_H is the Hall mobility, and PF is the theoretical power factor.

Reference

1. He, S. Y., Li, Y. B., Liu, L., et al. (2020). Semiconductor glass with superior flexibility and high room temperature thermoelectric performance. Sci. Adv. ***6***, eaaz8423.
2. Liang, X. and Chen, C. (2021). Ductile inorganic amorphous/crystalline composite Ag_4TeS with phonon-glass electron-crystal transport behavior and excellent stability of high thermoelectric performance on plastic deformation. Acta Mater. ***218***, 117231.
3. Yang, S. Q., Gao, Z. Q., Qiu, P. F., et al. (2021). Ductile $Ag_{20}S_7Te_3$ with Excellent Shape-Conformability and High Thermoelectric Performance. Adv. Mater. ***33***, 2007681.